Biomass Conversion and Biorefinery (2024) 14:4759–4776
https://doi.org/10.1007/s13399-022-02753-1

ORIGINAL ARTICLE

Synthesis and characterization of ferric@nanocellulose/nanohydroxyapatite bio-composite based on sea scallop shells and cotton stalks: adsorption of Safranin-O dye

Walaa A. Shaltout[1] · Gehan A. El-Naggar[1] · G. Esmail[1] · Asaad F. Hassan[1]

Received: 18 January 2022 / Revised: 23 April 2022 / Accepted: 27 April 2022 / Published online: 14 May 2022

Abstract
In the present study, four solid adsorbents were prepared via green synthesis sources, namely, nanohydroxyapatite (NHAP), nanocellulose (NC), nanocellulose/nanohydroxyapatite composite (NPC), and ferric@nanocellulose/nanohydroxyapatite composite (FNPC). Synthesis procedures were based on natural sources such as sea scallop shells and cotton stalks. All the prepared solid adsorbents were characterized by TGA, XRD, nitrogen adsorption/desorption isotherm, FTIR, pH_{PZC}, SEM, and TEM. FNPC exhibited a higher surface area (358.32 m^2/g), mesoporous surface (pore diameter, 12.29 nm), TEM particle size of 45 nm, and the availability of various surface functional groups. Static adsorption of Safranin-O (SO) dye was investigated for all the prepared solid adsorbents under different application conditions. Maximum adsorption capacity (239.23 mg/g) was achieved by FNPC after 24 h of equilibrium time, at pH 7, 2 g/L as adsorbent dosage, and 40 ℃. Adsorption of Safranin-O onto all the samples well-fitted Langmuir, Temkin, Freundlich, Dubinin–Radushkevich, pseudo-second-order, and Elovich models. Thermodynamic and kinetic parameters proved that Safranin-O adsorption is favorable, spontaneous, endothermic, and physisorption. Desorption studies confirmed that hydrochloric acid (0.03 mol/L) achieved the maximum desorption efficiency (92.8%). Reusability of FNPC showed a decrease in the adsorption capacity after five cycles of adsorption and desorption by only 7.8%.

Keywords Sea scallop shells · Cotton stalks · Nanocellulose · Nanohydroxyapatite · Safranin-O · Adsorption

1 Introduction

Recently, the treatment of wastewater particularly in chemical industries has been increasing attention. The growth of paper, wood, cosmetics, rubber, plastics, leather, and textile processing has resulted in environmental problems caused by carcinogenic and toxic contaminants, especially colored organic dyes, in discharged wastewater. A small amount of organic dyes in wastewater is highly toxic and visible to aquatic life; the effluents of dyes inhibit sunlight penetration into water which harms the ecosystem. It is difficult to treat water from dyes with microorganisms and chemical agents due to their stability against the biological and chemical degradations and complex molecular structure [1]. Safranin-O (SO) is a water-soluble cationic azine dye that is widely used in leather, textile, food, and pharmaceutical industries. It is known to be a reason for various health problems like skin infection, irritation in the respiratory system, eye irritation, allergies, and digestive tract infection when it is ingested, leading to diarrhea, nausea, and vomiting [2]. Thus, it is necessary to remove SO dye from the wastewater to make it useable and safe. Wastewater treatment technologies such as coagulation and flocculation [3], ultrafiltration [4], ion exchange [5], photocatalytic degradation [6], biological treatment [7], and adsorption [8–10] have been employed to eliminate dyes from wastewater. The adsorption technique is considered the most effective method due to its potential efficiency, high selectivity at the molecular level, low energy consumption, reusability, low cost, and easy operation. The adsorption of Safranin-O by using several adsorbents such as granular activated carbon [2], Khulays natural bentonite [11], natural zeolite [12], *Bambusa tulda* [13], and lignin nanoparticles [14] has been investigated. Nanoparticles offer a higher possibility for efficient adsorption of organic

✉ Asaad F. Hassan
asmz68@sci.dmu.edu.eg

[1] Chemistry Department, Faculty of Science, Damanhour University, Damanhour, Egypt

and inorganic pollutants as ideal adsorbents because of their unique properties such as recyclable, environmentally benign, efficient, selective, high surface area, and maximum adsorption capacity at a lower dosage. Several nanoparticles have been employed in adsorption such as iron, manganese oxide, zinc oxide, and carbon nanotubes [15].

Nanohydroxyapatite (NHAP) [$Ca_{10}(PO_4)_6(OH)_2$] is a nanomaterial with excellent nontoxicity bioactivity and biocompatibility. NHAP is widely used in dentistry and bone repair applications since it reflects a very good performance because of its similarity with the calcium phosphate mineral in the biological hard tissue [16]. Several methods have been applied for the synthesis of nanohydroxyapatite such as sol–gel synthesis [17], hydrothermal process [18], and aqueous chemical precipitation [19]. Green synthesis is vital for the environmental recovery, minimization of useless by-products, and less production cost of adsorbents compared to the expensive chemical synthesis. Biologically derived natural substances such as nacre, corals, animal bones, fishbone, eggshells, and scallop shells have been converted into beneficial nanohydroxyapatite. NHAP is an ideal material for the elimination of organic dyes because of its high adsorption capacity, thermal stability, surface activity, crystallinity, availability, water insolubility, and high porosity. The adsorption properties of NHAP possess great importance for both industrial purposes and environmental processes. NHAP needs to be modified to improve its efficiency and for easy and effective separation from the solution after the adsorption process [1]. Nanocellulose is the most abundant natural raw polymer with a total production of 10^{11}-10^{12} tones/year. Natural sources like cotton may include as high as nearly 98% of cellulose, some kinds of wood may contain almost 90%, and date seeds have 23.9%. Nanocellulose is biodegradable, cheap, non-toxic, renewable, tough, fibrous, water insoluble, and non-meltable and helps in maintaining the cell wall structure of oomycetes, algae, and plants [20]. This raw material can be used as an adsorbent in several forms like raw cellulose or modified cellulose to eliminate contaminants such as dyes, metals, phenols, and pesticides from water. The adsorption reactivity of nanocellulose is related to abundant -OH groups and can be increased by convenient modification either with surface groups or the formation of new composites. Ferric chloride can be used to modify solid adsorbents, whereas ferric ions are considered as Lewis acid which enhances the adsorption of basic dyes such as methylene blue, Safranin-O, crystal violet, and toluidine blue. Bi- and triple-composites possess unique properties such as high thermal stability, high adsorption capacity, suitable crystallinity, high specific surface area, highly porous nature, the presence of different active sites, and perfect morphology for achieving the best water treatment. It is the first time that nanocellulose was prepared from cotton stalks, and also, green material as a bio-composite was prepared from two natural solid wastes as sea scallop shells and cotton stalks in the same article and, then, decorated with ferric ions. It is considered a very promising solid material in environmental applications, especially the removal of effluent compositions.

The purpose of this work is the synthesis of four adsorbents, namely, nanohydroxyapatite (NHAP) that was prepared from sea scallop shells, nanocellulose (NC) that was obtained from cotton stalks, nanocellulose/nanohydroxyapatite composite (NPC), and ferric@nanocellulose/nanohydroxyapatite composite (FNPC). The prepared solid adsorbents were characterized by TGA, XRD, N_2 adsorption, FTIR, pH_{PZC}, SEM, and TEM techniques. The adsorption of Safranin-O from an aqueous solution was investigated under different adsorption conditions such as the effect of adsorbent dosage, pH of solution, shaking time, initial adsorbate concentration, and temperature. Kinetic and thermodynamic parameters were determined to understand the mechanism and nature of SO adsorption. Safranin-O desorption from the surface of FNPC was studied using several desorbing agents, and FNPC reusability was investigated after five cycles of the adsorption process.

2 Materials and methods

2.1 Materials

Sea scallop shells were gathered from Damietta sea beach, Egypt, and washed with distilled water. After washing, sea scallop shells were dried in an oven at 115 ℃ and ground into very small particles by Retsch ZM200 titanium mill. Cotton stalks were obtained from Egyptian farms, washed with distilled water to eliminate dirt, air-dried, and then ground into fine powder. Safranin-O (SO) was purchased from Loba Chemie Pvt. Ltd., Co. India. Diammonium hydrogen phosphate and hexahydrate ferric chloride were purchased from Oxford Lab Fine Chem Llp Co., India, while sodium hypochlorite, chloroform, ethanol, sulfuric acid, nitric acid, sodium hydroxide, ammonium hydroxide, and hydrochloric acid were purchased from El-Nasr for Pharmaceutical and Chemical Industry Co, Egypt.

2.2 Synthesis of solid adsorbents

2.2.1 Synthesis of hydroxyapatite nanoparticles from sea scallop shells

The resulted scallop shell powder was sintered in a muffle furnace at 900 ℃ for 3 h to transform calcium carbonate ($CaCO_3$) into calcium oxide (CaO) and decay all proteins and organic compounds. Four grams of the previous CaO powder was mixed with 1.5 mol/L HNO_3 to form

$Ca(NO_3)_2$ under continuous stirring. Solution of diammonium hydrogen phosphate (0.5 mol/L) was slowly dropped to the previous solution under magnetic stirring, and then 1.67 Ca/P ratio was achieved. The reaction mixture was retained at pH value of 10 using ammonium hydroxide solution overnight. Next, the precipitate was filtered from the solution, repeatedly washed with distilled water, and dried at 100 ℃ overnight. The formed powder was calcined at about 800 ℃ for 4 h to obtain nanohydroxyapatite (NHAP). The following equations express the included reactions [21]:

$$CaCO_3 \rightarrow CaO + CO_2 \quad (1)$$

$$CaO + 2HNO_3 \rightarrow Ca(NO_3)_2 + H_2O \quad (2)$$

$$10Ca(NO_3)_2 + 6(NH_4)_2HPO_4 + 8NH_4OH \rightarrow (Ca)_{10}(PO_4)_6(OH)_2 + 20NH_4(NO_3) + 6H_2O \quad (3)$$

2.2.2 Synthesis of nanocellulose

Forty grams of cotton stalk powder was added into 400 mL of 17.5% NaOH solution for the delignification and heated at 90 ℃ on a hot plate for 3 h under continuous stirring. The resulted delignified slurry was filtered, washed with distilled water till the solution becomes neutral, and dried for 48 h at room temperature. The dried delignified stalks were then bleached using 12% sodium hypochlorite (NaClO) solution at 80 ℃ for 45 min. The bleached stalks were washed with distilled water till reaching a neutral pH and were freeze-dried to a constant weight. The dried product was hydrolyzed with 100 mL of 2.5 mol/L HCl at 107 ℃ for 45 min under magnetic stirring. The hydrolyzed stalks were washed until the neutral filtrate solution and followed by dialysis process against distilled water for 2 days. The dialyzed cellulosic solution was freeze-dried and stocked in a refrigerator for later use. Nanocellulose (NC) was obtained as a snowy white powder [22].

2.2.3 Synthesis of nanocellulose/nanohydroxyapatite composite

One gram of NC was added into 100 mL of 10% NaOH solution at 4 ℃ for 1 h with magnetic stirring until dissolving nanocellulose and then mixed with 1 g of NHAP till formation of a homogenous solution. The pH of solution was adjusted to nearly 7 with 2 mol/L sulfuric acid at room temperature for precipitating the nanocellulose/nanohydroxyapatite composite (NPC). The precipitated composite was filtered, washed with distilled water, and dried at 80 ℃ [23].

2.2.4 Synthesis of ferric@nanocellulose/nanohydroxyapatite composite

One gram of NPC was added into 100 mL of 200 mg/L ferric chloride solution for 48 h under continuous stirring. The resulted composite was filtered, gently washed, and dried at room temperature (FNPC).

2.3 Characterization of the prepared solid adsorbents

Thermogravimetric analysis for NHAP, NC, NPC, and FNPC was employed using a thermal analyzer (SDT Q600 V20.9 Build 20) at a nitrogen flow rate of 50 mL/min and a temperature up to 800 ℃.

The crystalline characteristics of the prepared samples were determined by powder X-ray diffractometer (D8 advance diffractometer) at 40 mA and 40 kV. The sample was prepared by placing about 15 mg of fine ground sample into the sample holder and gently pressing on unglazed paper to minimize the preferred orientation. The XRD patterns were resulted from step scanning from 0 to 70˚ (2θ) at 0.01˚ or 0.02˚ increments.

The crystallinity index (I_{cr}) of the solid samples was evaluated by Equation 4 [24]:

$$I_{cr} = \frac{I_m - I_{am}}{I_m} \times 100 \quad (4)$$

where I_m and I_{am} represent the intensity of the main peak (at 2θ = 29.3, 22.1, 32.1, and 32.2) and the intensity of the amorphous peak (at 2θ = 40.4, 18.0, 21.9, and 22.0) for NHAP, NC, NPC, and FNPC, respectively.

Textural characterization for all the solid adsorbents was performed by a NOVA 3200e gas sorption analyzer (Quantachrome Corporation, USA) at –196 ℃ to investigate total pore volume (V_T), average pore diameter ($\bar{r}$), and specific surface area (S_{BET}). For the sample preparation, about 0.15 g of sample was placed into a dry and clean sample holder, and then the temperature was raised to 150 ℃ and degassed for a definite time (usually between 20 and 24 h) under reduced pressure of 10^{-5} Torricelli.

FTIR spectrophotometer was investigated for the solid samples before and after the SO adsorption in the range of 400–3800 cm^{-1} by Mattson 5000 FTIR spectrometer. The sample was prepared as follows: a small amount of sample (~10 mg) was mixed with about 25 to 30 times from its volume of KBr solution in an agate mortar and then pressed at 3000 kg/cm^2 for 3 min. The produced disc was

run on Nic-Plan FTIR microscope and set with a resolution of 8 cm^{-1} at 32 scans.

Point of zero charges of NHAP, NC, NPC, and FNPC was studied by adding 25 mL of 0.1 mol/L NaCl in several closed bottles. The initial pH (pH_i) values were adjusted between 4 and 12 by using 0.05 mol/L HCl and/or NaOH. The bottles were mixed with 0.025 g of solid samples and shaken for 24 h. The final pH (pH_f) values were investigated using a pH meter. The pH_{PZC} is the point at which $pH_f = pH_i$ [25].

Scanning electron microscope (SEM) was applied for NHAP, NC, NPC, FNPC, and SO adsorbed FNPC (SO-FNPC) using a JEOL JSM-6510LV model. The samples for SEM study were prepared by direct deposition of sample on an aluminum holder and then followed by sputter coating with a thin gold layer with an accelerating voltage of 15 kV under a high vacuum to provide a homogeneous surface for the correct analysis and imaging.

Transmission electron microscopy (TEM) was studied for NHAP, NC, NPC, and FNPC using a JEOL-JEM-2100 model and operating at 200 kV. Approximately, 10 mg of the sample was dispersed in ethanol for 45 min using sonication and then transferred to a copper grid. The sample was then taken to dry in the vacuum desiccator for 24 h before commencing the measurements.

2.4 Adsorption studies

The adsorption of Safranin-O from aqueous solution by NHAP, NC, NPC, and FNPC was performed by agitating 25 mL of SO solution having a definite concentration with 0.05 g of the solid adsorbent at 25 ℃ for 24 h and pH 7 value. The supernatant was filtered by using Whatman filter paper (Grade 1), the first 15 mL from the filtrate was rejected, and the unadsorbed SO concentration was determined at a wavelength of 532 nm by a UV-Vis spectrophotometer. The standard calibration curve for the calculation of Safranin-O concentration was prepared in the range of 1–14 mg/L with a higher correlation coefficient (0.9985) and presented in Fig. S1a. The systematic errors for the concentration measurements by UV-vis spectrophotometer were ∓ 0.1%. The measurements were repeated three times, and the average values of concentration were used. The error bars from both systematic and experimental errors were calculated and illustrated in the figures. The equilibrium adsorption capacity q_e (mg/g) was calculated using Eq. 5:

$$q_e = \frac{C_i - C_e}{\mathrm{m}} \times V \tag{5}$$

where C_e and C_i (mg/L) are the equilibrium and initial SO concentration, respectively, V is the SO solution volume (L), and m is the adsorbent mass (g). Different adsorption conditions were applied to study the effect of adsorbent dosage (0.2–2.2 g/L), pH (2–10), shaking time (2–30 h), initial SO concentration (40–700 mg/L) based on the adsorption capacity of solid samples, and studied adsorption temperature (25, 32, and 40 ℃).

2.5 Adsorption kinetic models

Mechanism and rate of Safranin-O adsorption onto the prepared adsorbents were studied by the linear form of pseudo-first order (PFO, Eq. 7), pseudo-second order (PSO, Eq. 10), and Elovich (Eq. 12) kinetic models [26]:

$$q_t = q_e(1 - e^{-k_1 t}) \tag{6}$$

$$\ln\left(q_e - q_t\right) = \ln\left(q_e\right) - k_1 t \tag{7}$$

$$q_t = \frac{\left(C_i - C_t\right)V}{m} \tag{8}$$

$$q_t = \frac{q_e^2\, k_2\, t}{1 + q_e\, k_2\, t} \tag{9}$$

$$\frac{t}{q_t} = \frac{1}{k_2\, q_e^2} + \frac{t}{q_e} \tag{10}$$

$$q_t = \frac{1}{\beta}\ \ln\left(1 + \propto \beta\ t\right) \tag{11}$$

$$q_t = \frac{1}{\beta} \ln\ \propto \beta + \frac{1}{\beta} \ln\ t \tag{12}$$

where q_t and q_e (mg/g) are the amounts of Safranin-O adsorbed (mg/g) at time t (h) and at equilibrium, respectively. C_t (mg/L), k_1 (h^{-1}), and k_2 (g/mg.h) are the residual SO concentration at time t, the rate constants of PFO, and PSO models, respectively. ∝ (mg/g.h) and β (g/mg) represent the initial rate of SO adsorption and the extent of surface coverage, respectively.

2.6 Adsorption isotherm models

Linear Langmuir isotherm (Eq. 14) assumes monolayer adsorption of adsorbates onto a homogeneous surface without interaction between the adsorbed species and is expressed as follows [27]:

$$q_e = \frac{b\ q_m C_e}{1 + b\ C_e} \tag{13}$$

$$\frac{C_e}{q_e} = \frac{1}{bq_m} + \frac{C_e}{q_m} \tag{14}$$

where q_m (mg/g) and b (L/mg) are the maximum adsorption capacity and Langmuir constant, respectively. Dimensionless separation parameter (R_L) was determined to explain the nature of SO adsorption, if it is unfavorable ($R_L > 1$), favorable ($0 < R_L < 1$), or irreversible ($R_L = 0$):

$$R_L = \frac{1}{1 + bC_i} \tag{15}$$

Linear Freundlich isotherm (Eq. 17) describes monolayer and multilayer adsorption on heterogeneous surfaces and is explained by the following equation [28]:

$$q_e = K_F C_e^{\frac{1}{n}} \tag{16}$$

$$\ln\ q_e = \ln\ K_F + \left(\frac{1}{n}\right)\ \ln\ C_e \tag{17}$$

where n and K_F ($L^{1/n}$. $mg^{1-1/n}$. g^{-1}) are Freundlich coefficients expressing the adsorption intensity and adsorption capacity, respectively.

The linear form of Temkin model (Eq. 19) describes the effect of indirect adsorbate–adsorbent interactions; the heat of adsorption decreases linearly instead of logarithmic with surface coverage, and is expressed by [29]

$$q_e = A\ \ln\ K_T\ C_e \tag{18}$$

$$q_e = A\ \ln\ K_T + A\ \ln\ C_e \tag{19}$$

$$A = \frac{RT}{b_T} \tag{20}$$

where A, R, and T are constants related to the adsorption heat, the gas adsorption constant (8.314 J/mol.K), and the absolute temperature in Kelvin, respectively. K_T(L/g) and b_T(J/mol) are Temkin constants.

The linear form of Dubinin–Radushkevich model (Eq. 23) is employed to distinguish between the adsorption on heterogeneous and homogeneous surfaces. The linear form is described as [30]

$$q_e = q_{DR}\ e^{-K_{DR}\varepsilon^2} \tag{21}$$

$$\varepsilon = RT\ \ln\left(1 + \frac{1}{C_e}\right) \tag{22}$$

$$\ln\ q_e = \ln\ q_{DR} - K_{DR}\ \varepsilon^2 \tag{23}$$

where ε represents the Polanyi potential, R is the gas constant, and T is the Kelvin temperature. q_{DR} (mg/g) and K_{DR} (mol^2/kJ^2) are the maximum adsorption capacity and Dubinin–Radushkevich constant, respectively. The mean adsorption free energy (E_{DR}, kJ /mol) is derived by

$$E_{DR} = \frac{1}{\sqrt{2K_{DR}}} \tag{24}$$

2.7 Thermodynamic studies

Adsorption thermodynamic parameters such as enthalpy ($\Delta H°$, kJ/mol), entropy ($\Delta S°$, kJ/mol.K), and free energy ($\Delta G°$, kJ/mol) changes were calculated using the following equations [25]:

$$K_d = \frac{C_s}{C_e} \tag{25}$$

$$\Delta G° = -RT\ \ln\ K_d \tag{26}$$

$$\ln\ K_d = \frac{\Delta S°}{R} - \frac{\Delta H°}{RT} \tag{27}$$

where C_e and C_s (mg/L) are the equilibrium concentrations of SO in the solution and on the adsorbent, respectively.K_d, T (K), and R are the adsorption distribution constant, the absolute temperature, and gas constant, respectively. $\Delta H°$ (kJ/mol) and $\Delta S°$ (kJ/mol.K) values were calculated from the slope and intercept of Van't Hoff plot (Eq. 27).

2.8 Safranin-O desorption and solid adsorbent reusability

The desorption process was studied by mixing 0.2 g of the dried SO pre-loaded FNPC with 100 mL of distilled water, acetic acid (0.03 mol/L), hydrochloric acid (0.03 mol/L), sulfuric acid (0.03 mol/L), or ethanol (95%) and then shaking for 10 h at 30 ℃. The desorbed SO concentration in the filtrate was investigated after filtration. Desorption efficiency% was determined using the following equation [31]:

$$\text{Desorption efficiency } \% = \frac{V\ C_d}{q\ m} \times 100 \tag{28}$$

where C_d (mg/L) is the equilibrium SO dye concentration after desorption from FNPC. V (L) is the desorbing agent volume. q (mg/g) is the maximum adsorption capacity of FNPC adsorbent. m (g) is the solid adsorbent weight.

Adsorbent reusability was carried out after five cycles of Safranin-O adsorption/desorption treatments. Adsorption of the dye was carried out by FNPC under 2 g/L as adsorbent dosage, pH 7, 600 mg/L as dye concentration, 24 h of shaking time, and at 25 °C. After each cycle, the solid adsorbent was filtered and washed several times with 30 mL of 0.03 mol/L HCl to desorb the pre-adsorbed dye, washed with distilled water, and dried at 80 °C for the successive reuse.

3 Results and discussion

3.1 Characterization of the solid adsorbents

Thermogravimetric analysis curves for NHAP, NC, NPC, and FNPC are presented in Fig. 1a. NHAP, NC, NPC, and FNPC showed total weight loss 7.2, 87.5, 46.6, and 36.0%, respectively. The total weight loss of nanohydroxyapatite up to 800 ℃ is due to the release of physically and chemically adsorbed water. Inorganic NHAP polymer remained undegraded, exhibiting the highest thermal stability [21]. The first weight loss for NC, NPC, and FNPC (5.8, 4.6, and 6.0%, respectively) up to 110 ℃ is related to the removal of moisture and residual solvents. Moreover, the previous three solid adsorbents showed high stability between 110 and 240 ℃. The substantial weight reduction (79.1%) for NC between 240 and 450 ℃ indicated the cellulose degradation, initiating with the dehydration, decomposition of glycosidic units, depolymerization, and decarboxylation. The final breakdown in NC from 450 to 580 ℃ is attributed to the combustion of char residue [22]. The residual weight (12.5% at 580 ℃) for nanocellulose contains levoglucosan and anhyrocellulose [32]. It was observed that the thermal stability of NPC and FNPC nanocomposites increased after the incorporation of NHAP. This could be related to the homogenous distribution of NHAP in the composites and the strong chemical interactions between NHAP, NC, and ferric ions [33]. Besides the hydrogen bonds in NPC structure, hydrophilic ferric cations were strongly crosslinked to NPC to form FNPC that exhibited higher thermal stability than NPC and enhanced its adsorption properties. The residual mass in the composites may represent higher amount of NHAP, since NHAP exhibited higher thermal stability at elevated temperature.

Figure 1b shows XRD patterns for all the solid samples. NHAP provided the characteristic peaks at 2θ of 25.8, 27.9, 29.3, 32.6, 34.4, 41.9, 47.1, and 53.1° associated to (002), (102), (210), (211), (202), (310), (222), and (004) planes, respectively (JCPDS card No. 09-0432) [34]. All the peaks are sharp, revealing that NHAP has high crystallinity and nanocrystal size, resulting in its high surface area [35]. The typical peaks of NC appeared at 2θ of 15.6, 22.1, and 33.8°, corresponding to (101), (002), and (040) planes related to type I of cellulose [24]. The crystallinity index was calculated by using Eq. 4, and the resulted data are listed in Table 1, indicating that the crystallinity index of NHAP, NC, NPC, and FNPC is about 94.1, 78.5, 87.3, and 82.9%, respectively. The high crystallinity of NC is ascribed to the reduction of the amorphous polymers lignin and hemicellulose from cotton stalks through the delignification and bleaching processes. The crystallinity index increased in NPC and FNPC compared with NC due to the inclusion of inorganic higher crystalline NHAP. The modification of NPC with ferric ions resulted in a decrease in FNPC crystallinity, compared with NPC, which may be related to the ion effect on the crystallization process of hydrogen bonding dominating inside the molecular structure of FNPC [36].

Surface area and porosity are important features for adsorbents. Figure 1c depicts the nitrogen adsorption isotherms, and the textural parameters for NHAP, NC, NPC, and FNPC are reported in Table 1. According to IUPAC classification, all the samples showed type II adsorption isotherms with H3-type hysteresis loops which include the monolayer–multilayer adsorption on mesoporous adsorbents with weak adsorbent–adsorbate interaction and aggregation of nanoparticles with slit-like pores [37]. Upon analysis of data summarized in Table 1, the specific surface area and total pore volume of FNPC > NPC > NHAP > NC confirm the highly porous nature of the resulted nanocomposites. The surface area increased from 81.76 to 358.32 m^2/g, indicating the availability of pores and active sites on NPC and FNPC surfaces and proving their higher adsorption capacity. The average pore diameter for NHAP (8.10 nm), NC (7.73 nm), NPC (8.00 nm), and FNPC (12.29 nm) was classified as mesopores.

Figure 1d displays FTIR spectra of NHAP, NC, NPC, and FNPC to study their surface chemical functional groups. NHAP has peaks at 450–498 and 559–606 cm^{-1} that belong to O-P-O doubly and triply degenerated bending modes, respectively. The bands for stretching vibration of phosphate groups were observed at 1037–1100 and 941–974 cm^{-1}, and their overtones are located at 2076 cm^{-1} [38]. No obvious bands of CO_3^{2-} group or organic compounds like C-H around 1350–1600 cm^{-1} proved the high NHAP purity [35, 39]. The apatitic -OH vibrational mode and -OH bending of adsorbed water appeared at 3450 and 1652 cm^{-1}, respectively. Nanocellulose showed characteristic peaks located at 667, 899, 1241, 1322, 1371, 1431, and 2901 cm^{-1} related to COH bending mode, (CCO, COC, and CCH) deformation modes of pure cellulose, C-O stretching of phenolics, COH vibration, C-H stretching, CH_2 bending vibration, and CH_3 groups, respectively. The peaks at 1060–1163 cm^{-1} are characteristic to saccharide structure in cellulose while the signals at 1640 and 3348 cm^{-1} to adsorbed water in carbohydrates and -OH stretching, respectively. All the previous

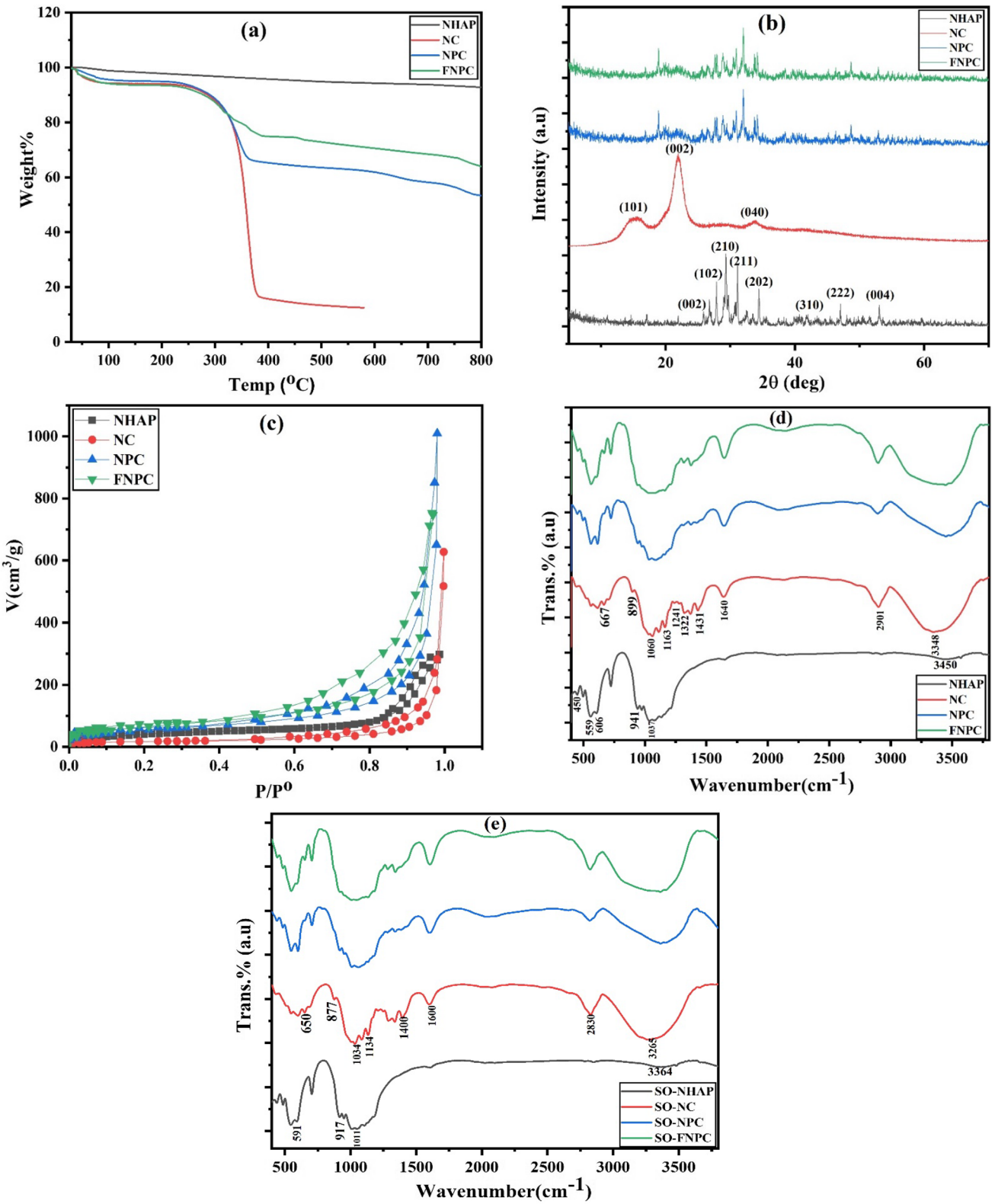

Fig. 1 TGA curves (**a**), XRD (**b**), nitrogen adsorption/desorption isotherms (**c**), and FTIR spectra before (**d**) and after SO adsorption (**e**) onto NHAP, NC, NPC, and FNPC

Table 1 Point of zero charge and textural parameters for NHAP, NC, NPC, and FNPC

Sample	pH_{PZC}	S_{BET} (m^2/g)	V_T (cm^3/g)	$\bar{r}$(nm)	I_{cr}
NHAP	7.3	211.24	0.428	8.10	94.1
NC	7.4	81.76	0.158	7.73	78.5
NPC	8.6	282.66	0.565	8.00	87.3
FNPC	8.1	358.32	1.101	12.29	82.9

bands indicate that the cellulose is type I, which is in agreement with XRD analysis. The absorption intensity of broad O-H bands increased in NPC and FNPC with a slight shift in the bands, indicating the establishment of hydrogen bonds between NHAP and NC [40]. Also, the crosslinking between ferric ions and hydroxyl groups of NPC composite was proven from the stretching of Fe-O-C bond at 1080 cm^{-1} and Fe-O bond at 563 cm^{-1},which are responsible for nanocomposite stability [36, 41]. Figure 1e shows FTIR spectra after the SO adsorption. The band around 3300 cm^{-1} displays the presence of $–NH_2$ group of Safranin-O. Also, the peak around 3000 cm^{-1} is due to –N-H group of SO. It was observed that the bands of the main adsorbents shifted and their transmittance decreased after the SO adsorption, proving the successful adsorption process [42, 43].

The calculated point of zero charge (pH_{PZC}) values for NHAP, NC, NPC, and FNPC is 7.3, 7.4, 8.6, and 8.1, respectively, as displayed in Fig. S1b and listed data in Table 1.

Figure 2a-d shows the SEM micrographs of the prepared solid samples (NHAP, NC, NPC, and FNPC), while SO adsorbed FNPC is displayed in Fig. S1c. Particles of nanohydroxyapatite had clearly defined spherical shape, small size, and agglutinated form. Nanocellulose surface depicted a regular porous nanostructure with homogeneously distributed individual crystalline particles due to the removal of amorphous components during the bleaching and delignification processes, which coincided with XRD and nitrogen adsorption data, confirming the ideal preparation of cellulose nanoparticles. In the case of NPC, we observed cohesively organized NC in NHAP structure with a systematic arrangement, evidencing the effective interaction between NHAP and NC [34]. Ferric ions caused shrinking and blanking of FNPC structure, decreasing the coagulation of particles, and producing more homogenous particles. In the case of SO adsorbed FNPC (Fig. S1c), Safranin-O was adsorbed by FNPC and aggregated over the pore cavity of FNPC. Also, Safranin-O appeared as white spots and showed a smooth surface [44].

TEM images are displayed in Fig. 2e, f, g and h for NHAP, NC, NPC, and FNPC, respectively, while TEM histogram is shown in Fig. S1d. TEM images indicate the better uniformity in the structure, porosity, shape, nano-sized particles, and distribution. NC showed a packed structure due to the existence of intramolecular and intermolecular hydrogen bonding and Van der Waals forces [22]. The average size of NHAP, NC, NPC, and FNPC is about 11, 15, 29, and 45 nm, respectively.

3.2 Adsorption of Safranin-O onto the solid adsorbents

3.2.1 Effect of nanoadsorbent dosage

The effect of increasing the applied adsorbent masses on the adsorption capacity to choose the suitable mass of adsorbent during the adsorption of Safranin-O was studied. Figure 3a depicts the effect of adsorbent dosage (0.2–2.2 g/L) on the adsorption capacity (q_e, Eq. 5) using 25 mL of 300 mg/L SO solution, for 24 h, and at 25 ℃. Increasing the adsorbent masses from 0.2 to 1.4 g/L is accompanied by a high increase in the adsorption capacity (3.0, 5.7, 1.9, and 2.3 times for NHAP, NC, NPC, and FNPC, respectively) due to the rapid increase of surface functional active adsorption sites with increasing the weight of the solid adsorbents [11]. Only about 7–14 mg/g increase was observed as the adsorbent dosage increased from 1.4 to 2.0 g/L. At adsorbent dosage > 2 g/L, there is no evident effect on the adsorption capacities owing to the equilibrium establishment at a lower SO concentration in the adsorption solution. According to the obtained results, 2 g/L was chosen as the optimum adsorbent dosage value.

3.2.2 Effect of pH

The pH of solution influences the adsorption process and determines the surface charge of adsorbent and the adsorbate state in the solution. The pH effect on the adsorption of cationic SO onto the solid adsorbents was performed by using pH in the range (2–10), 25 mL of 300 mg/L SO solution, 0.05 g of adsorbent, for 24 h, and at 25 ℃. Figure 3b displays the pH effect on the adsorption capacity (q_e, Eq. 5) of adsorbents where q_e increased from 18.7, 11.8, 29, 49 mg/g to 60.8, 39.2, 88.2, and 114 mg/g for NHAP, NC, NPC, and FNPC, respectively, through pH values from 2 to 10. This is related to the increase in electrostatic attraction between adsorbent sites and Safranin-O dye and, also, the decrease in protonation of the adsorbent surface with raising pH value ($pH > pH_{PZC}$). H_3O^+ ions competed with the cationic groups of SO dye at a lower pH ($pH < pH_{PZC}$), resulting in decreasing the removal percent [12]. From the previous results, the adsorption efficiency increased at the higher basic medium and decreased at the higher acidic medium, depending on

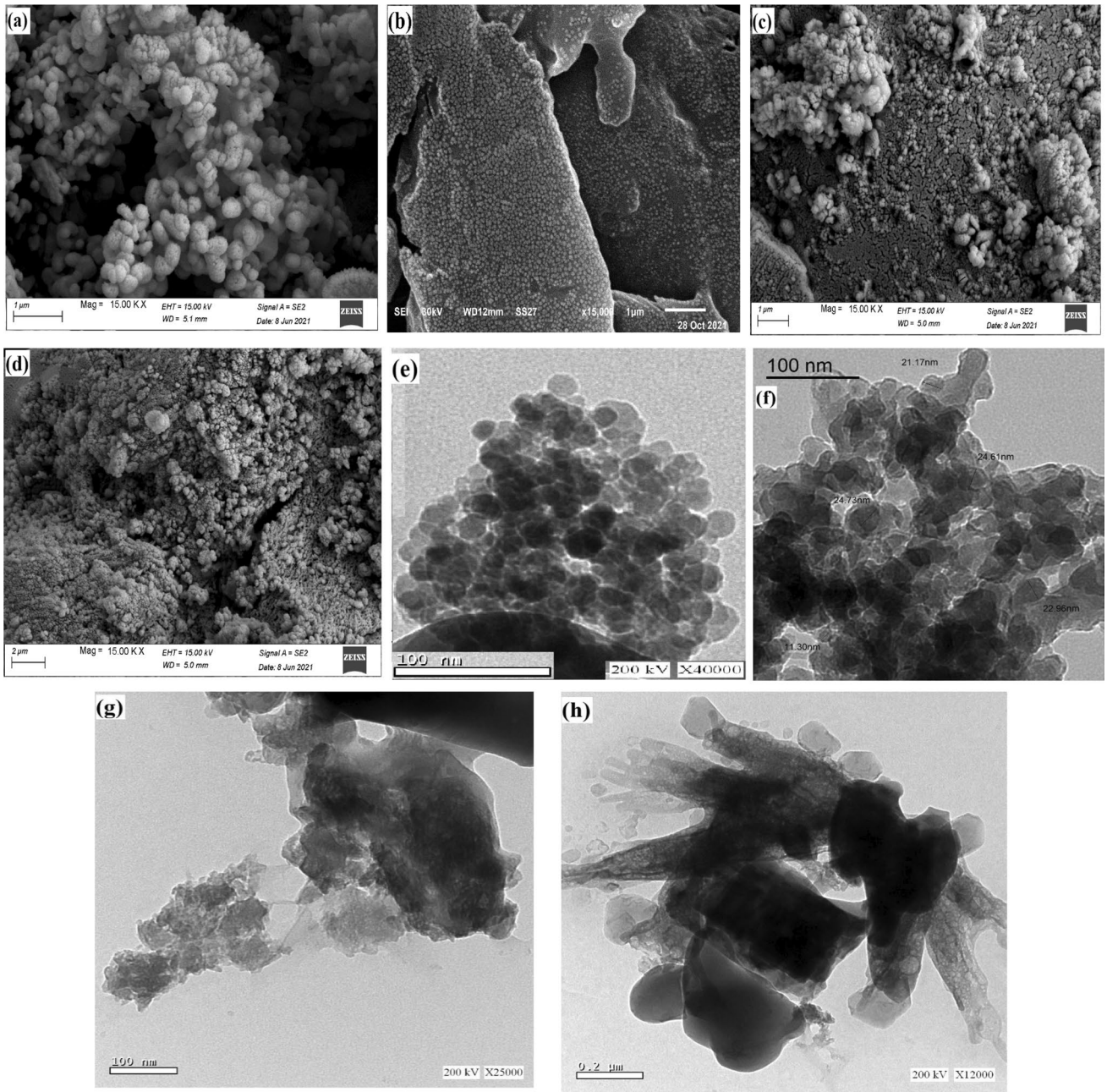

Fig. 2 SEM (**a**, **b**, **c**, and **d**) and TEM (**e**, **f**, **g**, and **h**) images for NHAP, NC, NPC, and FNPC, respectively

the pH_{PZC} (7.3, 7.4, 8.6, and 8.1 for NHAP, NC, NPC, and FNPC, respectively).

3.2.3 Effect of contact time and adsorption kinetic models studies

The effect of shaking time on the removal of cationic organic dyes by adsorption is an important factor to investigate the equilibrium time and adsorption kinetics. The optimum equilibrium time was studied by elucidating the contact time (h) against adsorption capacity (mg/g) at 25 ℃ in the range of 2–30 h as shown in Fig. 3c. The adsorption of SO sharply increased at the beginning time due to the abundance of adsorption active sites onto the solid adsorbents [8]. Safranin-O adsorption increased until adsorption equilibrium time was attained after 14 h for NHAP, NC, and NPC while after 20 h in the case of FNPC. After the equilibrium time, the uptake of SO remained unchanged due to the saturation of adsorbent surface with SO molecules. Figure 3d-e illustrates the PSO (Eq. 10) and Elovich (Eq. 12)

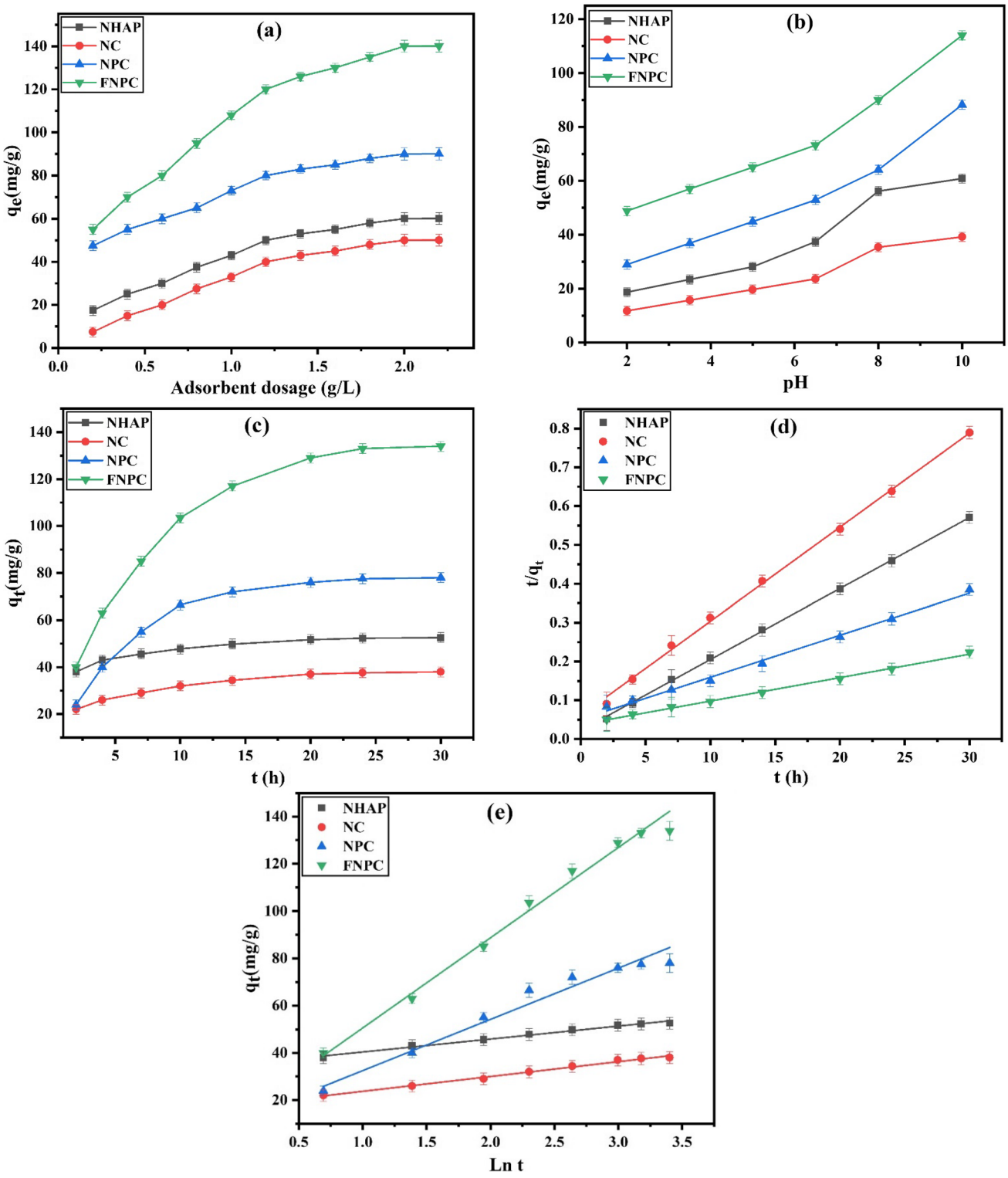

Fig. 3 Effect of nano-adsorbent dosage (**a**), pH effect (**b**), shaking time effect (**c**), pseudo-second order kinetic (**d**), and Elovich (**e**) plots for the adsorption of SO onto NHAP, NC, NPC, and FNPC at 25 ℃

linear plots, respectively, while PFO (Eq. 7) linear plot is represented in Fig. S2. Kinetic model parameters for SO adsorption onto the solid samples are reported in Table 2. Upon analysis of results in Table 2, (i) the adsorption of SO onto all the adsorbents fitted well the kinetic model of pseudo-second-order according to the slight difference

Table 2 Pseudo-first, pseudo-second order, Elovich kinetic models, and thermodynamic parameters for adsorption of SO onto NHAP, NC, NPC, and FNPC at 25 ℃

Models	Parameters		NHAP	NC	NPC	FNPC
PFO	q_m **(mg/g)**		59.59	40.68	96.06	132.45
	q_e **(mg/g)**		18.00	20.38	67.48	92.54
	k_1 **(** h^{-1}**)**		0.1583	0.1438	0.2164	0.1664
	R^2		0.9711	0.9827	0.9842	0.9832
PSO	q_e **(mg/g)**		54.59	41.02	92.94	137.80
	k_2 **(g/mg.h)**		0.0156	0.0102	0.0022	0.0010
	R^2		0.9996	0.9982	0.9945	0.9973
Elovich	α **(mg/g.h)**		318.19	101.20	38.24	54.67
	β **(g/mg)**		0.1824	0.1593	0.0478	0.0269
	R^2		0.9872	0.9909	0.9574	0.9862
Thermodynamic parameters	R^2		0.9941	0.9999	0.9611	0.9947
	ΔH° (kJ/mol)		31.00	22.27	34.54	32.31
	ΔS° (kJ/mol.K)		0.114	0.083	0.124	0.121
	−ΔG° (kJ/mol)	**25** ℃	3.104	2.367	2.195	3.726
		32 ℃	3.978	2.949	3.435	4.501
		40 ℃	4.822	3.608	4.055	5.538
	K_d	**25** ℃	3.50	2.60	2.42	4.50
		32 ℃	4.80	3.20	3.88	5.90
		40 ℃	6.38	4.00	4.75	8.40

between the Langmuir adsorption capacities (q_m) and calculated values (q_e) (8.4, 0.8, 3.2, and 3.9% for NHAP, NC, NPC, and FNPC, respectively), in addition to the higher correlation coefficients (0.9945–0.9996). (ii) Besides the high difference between q_e and q_m values (69.8, 49.9, 29.8, and 30.1% for NHAP, NC, NPC, and FNPC, respectively), the R^2 values (0.9711–0.9842) obtained from PFO model are less than that of PSO model, proving that Safranin-O adsorption onto the prepared samples did not follow PFO model. (iii) The rate constants (K_2) for PSO kinetic model located in the range 0.0010–0.0156 g/mg.h and the higher rate constants of NHAP and NC may be related to the higher attraction force between chemical functional groups present on the solid surface and the cationic SO dye. (iv) Coefficients of determination ($R^2 > 0.9574$) in Elovich model confirm the well fitted equation. α and β values present in the range between 38.24–318.19 mg/g.h and 0.0269–0.1824 g/mg, respectively, indicate that the adsorption equilibrium and surface coverage for NHAP and NC are confirmed in a very short time.

3.2.4 Effect of initial Safranin-O dye concentration

The equilibrium adsorption isotherm explains the behavior of interaction between the active sites of adsorbent and adsorbate ions. As analyzed in Fig. 4a-d, the effect of different adsorption temperatures (25, 32, and 40 ℃) on the removal of SO onto NHAP, NC, NPC, and FNPC was studied using 2 g/L of adsorbent mass, 24 h shaking time, pH 7, and 40–700 mg/L of initial SO concentration based on the adsorption capacity of solid samples. Figure 4a-d discusses that SO adsorption highly raised at a lower initial concentration, indicating that SO dye molecules had very high affinity for the prepared adsorbent surface, leading to complete adsorption in the diluted solution of dye. Adsorption was stable at a high initial concentration which is related to coverage of all the available active sites. Four isotherms, namely, Langmuir, Freundlich, Temkin, and Dubinin–Radushkevich models (Eqs. 14, 17, 19, and 23, respectively), were applied to illustrate the obtained experimental adsorption equilibrium results as reported in Table 3.

As displayed in Fig. 4e-h, adsorption of SO onto all the prepared solid adsorbents fitted well Langmuir adsorption model according to the higher correlation coefficients (0.9962–0.9998). Adsorption capacity of FNPC > NPC > NHAP > NC at 40 ℃ (239.23, 125.79, 81.37, and 51.79 mg/g, respectively), as at the other temperatures, is attributed to the incorporation of many chemical functional groups on FNPC surface. FNPC is characterized by its higher specific surface area (358.32 m^2/g) and the presence of many chemical functional groups which enhance the surface attraction of Safranin-O. The presence of Fe^{+3} as Lewis acidic groups raises the tendency to nitrogen Lewis basic groups of dye. The enhancement of adsorption capacities with the increase in temperature revealed the endothermic adsorption processes in all cases. The values of Langmuir binding constant (b, L/mg) that express the energy of adsorption follow the sequence NHAP > NC > NPC > FNPC at 40 ℃, implying the higher affinity of binding strength between NHAP and SO. Moreover, the

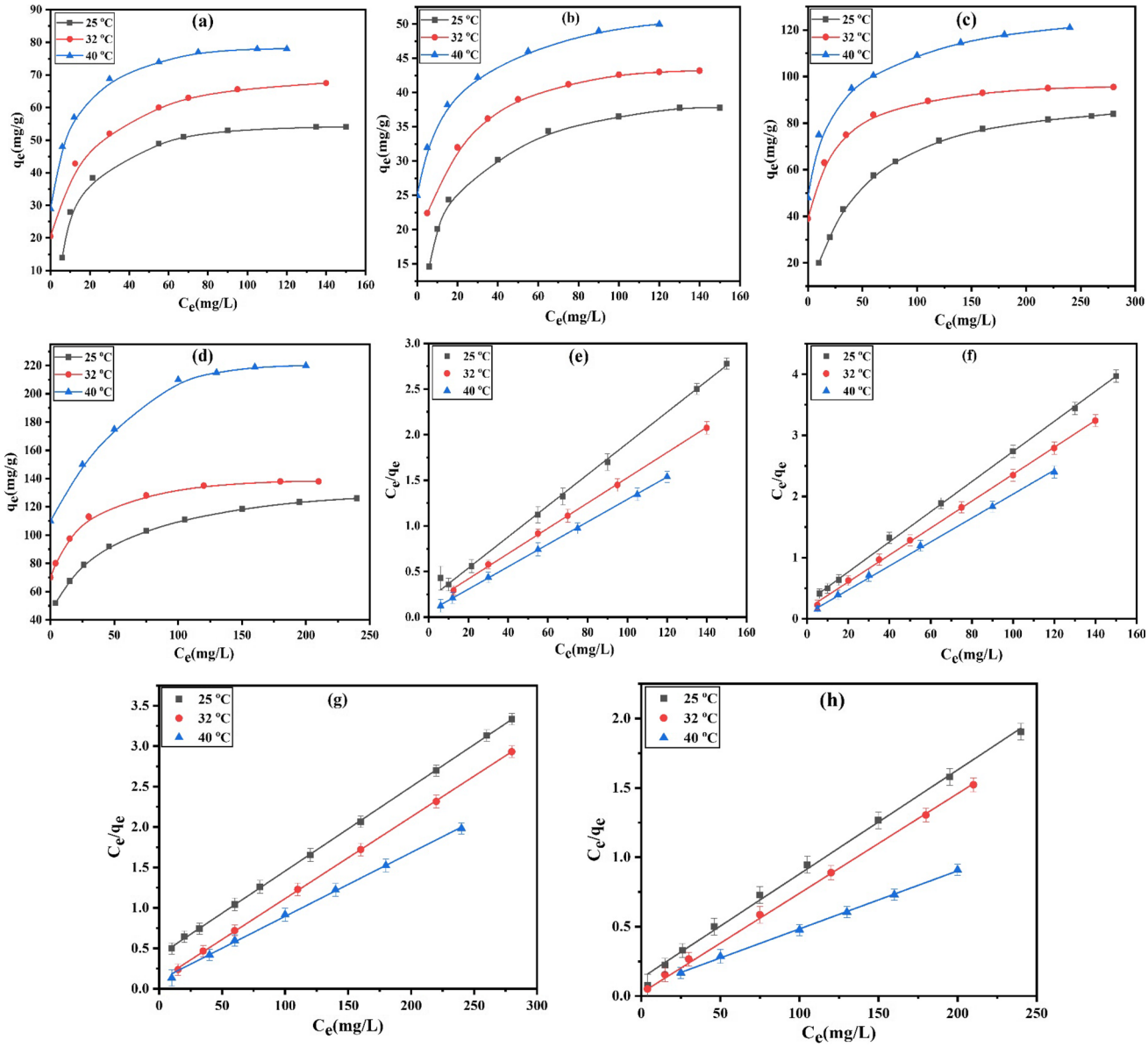

Fig. 4 Adsorption isotherms of SO (**a**, **b**, **c**, and **d**) and Langmuir plots (**e**, **f**, **g**, and **h**) for NHAP, NC, NPC, and FNPC, respectively at 25, 32, and 40 ℃

Safranin-O adsorption onto NHAP became stronger [29], and the results were also confirmed by α and β parameters calculated from Elovich kinetic model and rate constant of PSO model (K_2). Since NC possesses high crystallinity, the hydrophilic amorphous region that is responsible for the adsorption of water-soluble SO dye is less than the crystalline region, resulting in the low adsorption capacity of NC [45]. The R_L values that were calculated from Eq. 15 based on Langmuir constant are more than 0.0301 and less than unit, proving the favorable adsorption of SO onto the studied adsorbents.

Freundlich plots for SO adsorption onto NHAP, NC, NPC, and FNPC at 25, 32, and 40 ℃ are shown in Fig. S3a–d. Upon inspection of data in Table 3, the calculated R^2 values are higher than 0.9121, indicating the good application of Freundlich model. K_F values raised with temperature for all the samples as with q_m of Langmuir isotherm. The *1/n* values ranged between 0.1401 and 0.4135 ($0.1 < 1/n < 1.0$), confirming that the adsorption process is favorable, successful, and rapid. On the other hand, the *1/n* values are less than 1, pointing out physisorption mechanism [46].

Temkin isotherm model was studied at various temperatures (25, 32, and 40 ℃) as depicted in Fig. 5a-d to explain the adsorption of Safranin-O dye onto the synthesized solid adsorbents. The estimated equilibrium binding constants

Table 3 Langmuir, Freundlich, Temkin, and Dubinin–Radushkevich parameters for adsorption of SO onto NHAP, NC, NPC, and FNPC at 25, 32, and 40 ℃

Parameters	NHAP			NC			NPC			FNPC		
	25 ℃	**32** ℃	**40** ℃	**25** ℃	**32** ℃	**40** ℃	**25** ℃	**32** ℃	**40** ℃	**25** ℃	**32** ℃	**40** ℃
Langmuir												
q_m **(mg/g)**	59.59	72.41	81.37	40.68	45.54	51.79	96.06	99.11	125.79	132.45	142.04	239.23
b **(L/mg)**	0.0751	0.0964	0.2042	0.0891	0.1324	0.1898	0.0251	0.0952	0.0817	0.0624	0.1611	0.0642
R_L	0.1175	0.0940	0.0467	0.1009	0.0702	0.0501	0.1659	0.0499	0.0577	0.0742	0.0301	0.0722
R^2	0.9967	0.9993	0.9998	0.9994	0.9993	0.9987	0.9998	0.9998	0.9982	0.9962	0.9995	0.9991
Freundlich												
1/n	0.2394	0.1974	0.1622	0.2750	0.1982	0.1422	0.4135	0.1558	0.1478	0.2365	0.1401	0.1956
K_F ($L^{1/n}.mg^{1-1/n}.g^{-1}$)	17.538	26.521	37.548	10.303	17.148	25.770	9.217	44.715	53.447	36.433	68.482	81.434
R^2	0.9121	0.9709	0.9498	0.9337	0.9606	0.9936	0.9410	0.9454	0.9937	0.9909	0.9605	0.9525
Temkin												
b_T **(J/mol)**	231.46	235.65	253.80	347.64	394.18	449.96	123.82	224.41	176.13	123.57	256.11	174.03
K_T **(L/g)**	2.209	4.430	21.414	1.629	7.250	50.178	0.272	12.584	17.768	3.280	1221.935	1613.060
R^2	0.9464	0.9828	0.9698	0.9822	0.9853	0.9985	0.9909	0.9672	0.9984	0.9886	0.9038	0.9182
Dubinin–Radushkevich												
q_{DR}**(mg/g)**	55.23	68.84	79.45	38.51	43.44	49.75	85.80	96.70	122.86	125.47	140.32	224.63
E_{DR} **(kJ/mol)**	0.0915	0.0867	0.1266	0.0887	0.1158	0.1458	0.0352	0.0581	0.0522	0.0512	0.0782	0.0721
R^2	0.9947	0.9972	0.9562	0.9841	0.9806	0.9346	0.9936	0.9963	0.9778	0.9617	0.9954	0.9806

(K_T) raised with temperature, confirming the endothermic nature of adsorption and the improvement of adsorption at higher temperature [47]. The higher values of correlation coefficient (0.9038–0.9985) illuminate the great fitting of Temkin adsorption isotherm model. The Temkin parameters values ranged between 123.57 and 449.46 J/mol ($b_T < 8000$ J/mol), evidencing the dominance of physical adsorption [48].

Figure 5e-h represents the linear plots of Dubinin–Radushkevich model for SO adsorption onto the solid adsorbents at different temperatures, and data are summarized in Table 3. Besides the small variance (1.2–10.7%) between the adsorption capacities (q_{DR}) of Dubinin–Radushkevich model and q_m of Langmuir model, the higher regression coefficient values ($R^2 > 0.9346$) exhibited the perfect suitability of Dubinin–Radushkevich model. This isotherm model is used to differentiate between the chemical and physical nature of adsorption process using the mean energy values of adsorption (E_{DR}, kJ/mol). Whereas when E_{DR} values are less than 8 kJ/mol, the adsorption correlates to physical adsorption, but chemisorption is achieved if the values are in the range of 8–16 kJ/mol. As mentioned in Table 3, E_{DR} values lie between 0.0352 and 0.1458 kJ/mol, revealing the physisorption and monolayer–multilayer coverage of SO onto the prepared adsorbents at all the utilized temperatures [46, 49]. The previous data imply that SO adsorption onto NHAP, NC, NPC, and FNPC fitted well the four applied isotherm models at 25, 32, and 40 ℃. Moreover, the experimental isothermal data correlated with the data of Elovich and PSO kinetic models.

3.2.5 Thermodynamic parameters

The enthalpy change ($\Delta H°$) and entropy change ($\Delta S°$) for SO adsorption were calculated from Van't Hoff equation (Eq. 27, Fig. 6a), while the free energy change ($\Delta G°$) was evaluated using Eq. 26, and these parameters are listed in Table 2. Upon analysis of thermodynamic data in Table 2, (i) the positive change in $\Delta S°$ values ranged between 0.083 and 0.124 kJ/mol.K, reflecting that the organization of Safranin-O at the solid/solution interface became more random [49]. (ii) The positive enthalpy change values affirm the endothermic nature of the adsorption of Safranin-O onto the investigated samples. (iii) The negative $\Delta G°$ values prove the favorability and spontaneity of SO adsorption at all the temperatures onto all the prepared samples. (iv) The increase in positive K_d and negative $\Delta G°$ values with temperature showed the improved adsorption at a higher temperature. (v) The calculated $\Delta G°$ values in the range –2.195 to –5.538 kJ/mol indicate the physical adsorption process, where physisorption occurs at $\Delta G°$ values in the range from 0 to –20 kJ/mol, and the values of $\Delta G°$ for chemical adsorption are between – 400 and – 80 kJ/mol [47]. Further, the values of $\Delta H°$ lie between 22.27 and 34.54 kJ/mol (< 40 kJ/mol), implying the physisorption of SO onto the studied adsorbents [25]. (vi) The higher correlation coefficients (0.9611–0.9999) of Van't Hoff plot

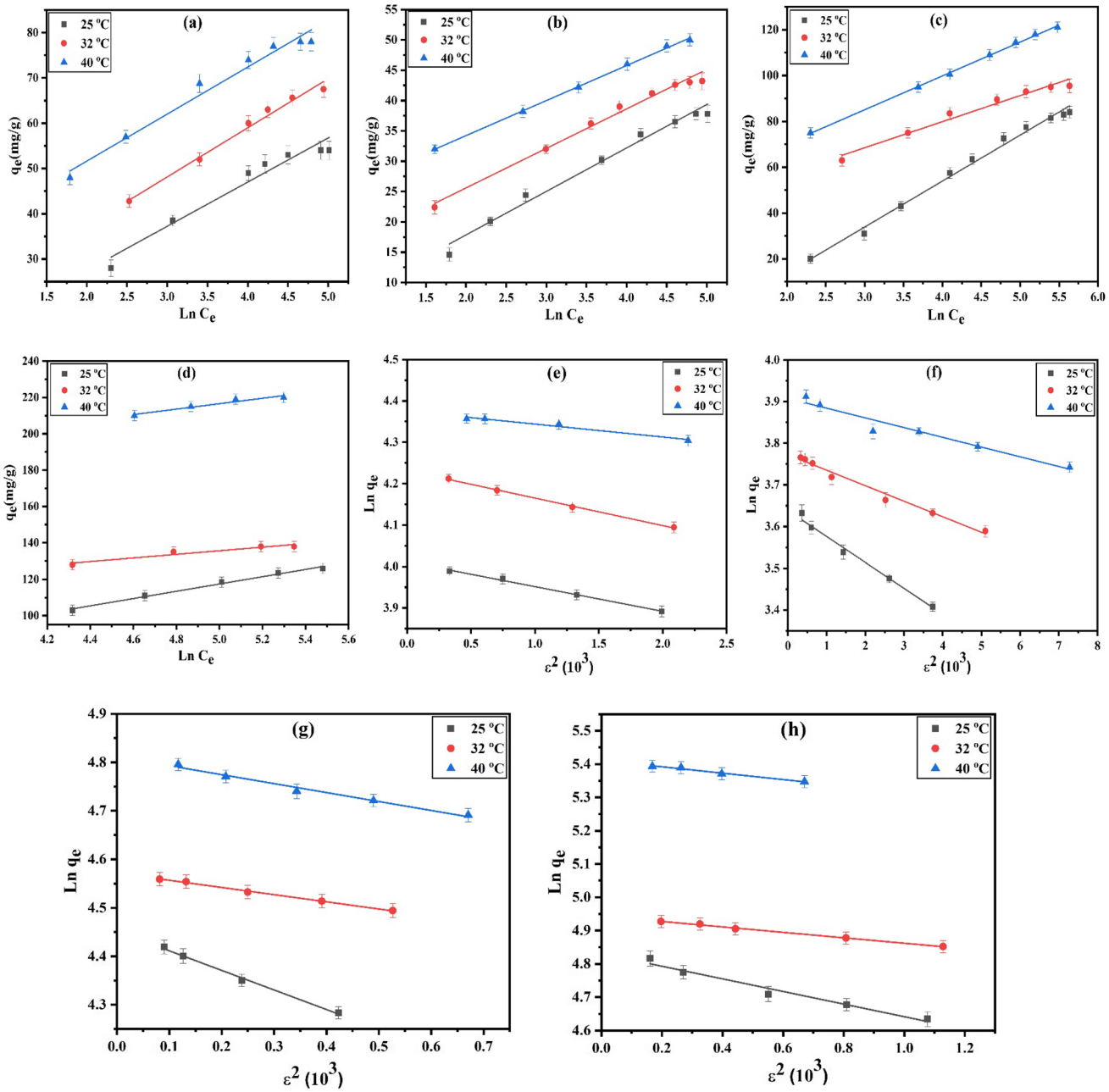

Fig. 5 Temkin (**a**, **b**, **c**, and **d**) and linear Dubinin–Radushkevich plots (**e**, **f**, **g**, and **h**) for the adsorption of SO onto NHAP, NC, NPC, and FNPC, respectively at 25, 32, and 40 ℃

confirm the good application of this model. (vii) ΔH° and ΔS° trend (NPC > FNPC > NHAP > NC) may be related to the increase in disorder and endothermic nature onto NPC surface. Also, ΔG° values at 32 and 40 ℃ for FNPC > NHAP > NPC > NC may belong to the more favorable spontaneous adsorption of SO onto FNPC surface compared with the other studied adsorbents.

3.3 Desorption study and solid adsorbent reusability

Figure 6b shows the desorption of SO from FNPC surface using different solvents, and desorption efficiencies (D.E%) were calculated by Eq. 28. It was observed the desorption efficiency for HCl (0.03 mol/L) > H_2SO_4

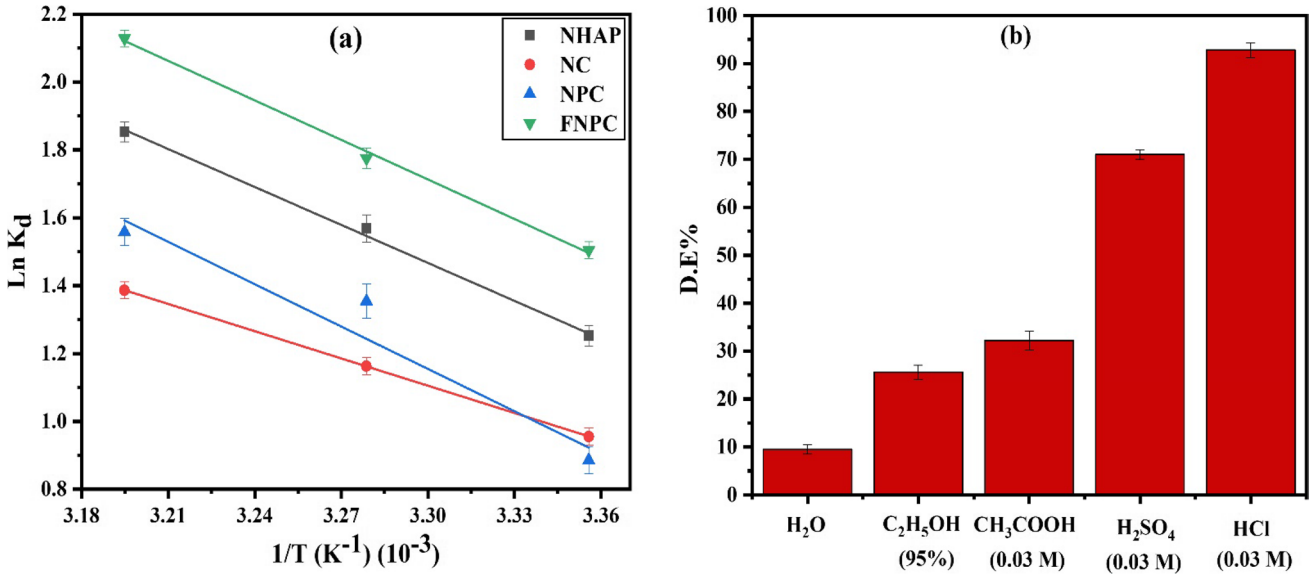

Fig. 6 Van't Hoff plot (**a**) for all the studied solid adsorbents and desorption of SO from FNPC using different solvents (**b**)

Table 4 Comparison of maximum Langmuir adsorption capacity of FNPC with other solid adsorbents

Adsorbents	Adsorption conditions	q_m (mg/g)	References
Heulandite	25 ℃, 4 h, pH 4	41.66	[12]
NBT	25 ℃, 1.5 h, pH 7	32.26	[13]
LN-g-PAA	25 ± 2 ℃, 3.75 h, pH 7	138.88	[14]
SDS/RM	35 ℃, 0.75 h, pH 4	89.47	[42]
Peanut shell-based polyurethane foam	60 ℃, 5 h, pH 9	23.58	[50]
Natural Iraqi palygorskite	27 ± 2 ℃, 0.5 h, pH 7	200.00	[51]
Soybean hull	50 ℃, 1.5 h, pH 8	29.49	[52]
SMABT	25 ℃, 24 h, pH 7	90.90	[53]
MSep nanocomposite	25 ℃, 0.5 h, pH 7	18.48	[54]
FNPC	40 ℃, 24 h, pH 7	239.23	[This study]

(0.03 mol/L) > CH_3COOH (0.03 mol/L) > C_2H_5OH (95%) > H_2O (92.8, 71.0, 32.2, 25.6, and 9.5%, respectively). HCl and H_2SO_4 (inorganic solvents) demonstrate the maximum desorption efficiency because the anionic functional groups of FNPC tend to adsorb the cationic protons of inorganic solvents but not the cationic groups of Safranin-O dye. Moreover, HCl and H_2SO_4 have higher polarity and protons than the other used solvents.

The reusability of FNPC was tested after five cycles of Safranin-O sorption as shown in Fig. S4. It is revealed that FNPC is reusable even after five cycles of adsorption/desorption where only 7.8% of its adsorption efficiency decreased. The decrease in adsorption efficiency may be related to the coagulation of solid adsorbent particles, which is responsible for the decrease in specific surface area and the expected loss of some surface chemical functional groups [30].

3.4 Comparison of FNPC with other adsorbents

The Langmuir adsorption capacity ($q_{m,}$ mg/g) value of FNPC for adsorption of SO is 239.23 mg/g at 40 ℃ that is higher than that of the various adsorbents mentioned in Table 4, considering the used adsorption conditions in each article [12–14, 42, 50–54]. We can conclude that FNPC as a green prepared material with a higher specific surface area (358.32 m^2/g), higher total pore volume (1.101 cm^3/g), and the presence of Lewis acidic surface chemical functional groups is a promising solid material for the removal of Safranin-O from wastewater.

4 Conclusion

Four nano-solid adsorbents, nanohydroxyapatite (NHAP), nanocellulose (NC), nanocellulose/nanohydroxyapatite composite (NPC), and ferric@nanocellulose/nanohydroxyapatite composite (FNPC), were successfully prepared from sea scallop shells for NHAP and cotton stalks for NC as by-products natural sources based on green synthesis procedures. The prepared solid nano-adsorbents were characterized by different physicochemical techniques and exhibited high thermal stability up to 800 and 350 ℃ in the case of NHAP and NC, respectively, high crystallinity (78.5–94.1%), porous nature, high specific surface area (81.76–358.32 m^2/g), and nano-structure. Adsorption of Safranin-O onto all the prepared solid materials was investigated, while FNPC exhibited the maximum adsorption capacity (q_m, 239.23 mg/g) at an adsorbent dosage of 2 g/L, 24 h of equilibrium shaking time, and 40 ℃. The incorporation of Lewis acidic centers (Fe^{+3}) on a higher specific surface area of composite will act as created attractive sites for SO ions from the aqueous medium. The adsorption process was well fitted with different adsorption, kinetic, and thermodynamic models which confirm the endothermic, spontaneous, physisorption, and favorable process. To investigate solid adsorbent sustainability, SO desorption was studied using different eluents from the surface of FNPC. Maximum desorption efficiency was confirmed by using 0.03 mol/L HCl (92.8%). The higher reusability of FNPC was tested after five cycles of SO adsorption/desorption and exhibited a decrease in its adsorption capacity by only 7.8%. The previous study concluded that nanocellulose/nanohydroxyapatite and its ferric decorated form are very promising solid materials in environmental applications; especially, it is green material prepared from natural solid waste as scallop shells and cotton stalks.

Supplementary Information The online version contains supplementary material available at https://doi.org/10.1007/s13399-022-02753-1.

Author contribution All authors contributed to the study conception and design. Material preparation, data collection, and analysis were performed by Walaa A. Shaltout, Gehan A. El-Naggar, G. Esmail, and Asaad F. Hassan.

Funding Open access funding provided by The Science, Technology & Innovation Funding Authority (STDF) in cooperation with The Egyptian Knowledge Bank (EKB).

Declarations

Conflict of interest The authors declare no competing interests.

References

1. Prabhu SM, Khan A, Hasmath Farzana M et al (2018) Synthesis and characterization of graphene oxide-doped nano-hydroxyapatite and its adsorption performance of toxic diazo dyes from aqueous solution. J Mol Liq 269:746–754. https://doi.org/10.1016/j.molliq.2018.08.044
2. Sharma K, Vyas RK, Singh K, Dalai AK (2019) Reactive adsorption of Safranin O: surface – pore diffusion modeling and degradation study. Water Sci Technol 80:665–674. https://doi.org/10.2166/wst.2019.317
3. Gadekar MR, Ahammed MM (2016) Coagulation/flocculation process for dye removal using water treatment residuals: modelling through artificial neural networks. Desalin Water Treat 57:26392–26400. https://doi.org/10.1080/19443994.2016.1165150
4. Bouazizi A, Breida M, Achiou B et al (2017) Removal of dyes by a new nano–TiO2 ultrafiltration membrane deposited on low-cost support prepared from natural Moroccan bentonite. Appl Clay Sci 149:127–135. https://doi.org/10.1016/j.clay.2017.08.019
5. Hassan MM, Carr CM (2018) A critical review on recent advancements of the removal of reactive dyes from dyehouse effluent by ion-exchange adsorbents. Chemosphere 209:201–219. https://doi.org/10.1016/j.chemosphere.2018.06.043
6. Subramanian H, Krishnan M, Mahalingam A (2022) Photocatalytic dye degradation and photoexcited anti-microbial activities of green zinc oxide nanoparticles synthesized via Sargassum muticum extracts. RSC Adv 12:985–997. https://doi.org/10.1039/d1ra08196a
7. Bhatia D, Sharma NR, Singh J, Kanwar RS (2017) Biological methods for textile dye removal from wastewater: a review. Crit Rev Environ Sci Technol 47:1836–1876. https://doi.org/10.1080/10643389.2017.1393263
8. Hassan AF, Elhadidy H (2017) Production of activated carbons from waste carpets and its application in methylene blue adsorption: kinetic and thermodynamic studies. J Environ Chem Eng 5:955–963. https://doi.org/10.1016/j.jece.2017.01.003
9. Lal P, Jitendra M, Saini K et al (2021) Fabrication of polyaniline - coated porous and fibrous nanocomposite with granular morphology using tea waste carbon for effective removal of rhodamine B dye from water samples. Biomass Convers Biorefinery. https://doi.org/10.1007/s13399-021-02267-2
10. Al TJ, Sayyed M, Ali M et al (2021) Adsorption of malachite green dye onto almond peel waste : a study focusing on application of the ANN approach for optimization of the effect of environmental parameters. Biomass Convers Biorefinery. https://doi.org/10.1007/s13399-021-02174-6
11. Al-Shahrani S (2018) Removal of Safranin dye from wastewater using Khulays natural bentonite. J King Abdulaziz Univ Sci 29:49–58. https://doi.org/10.4197/eng.29-1.4

12. Abukhadra MR, Mohamed AS (2019) Adsorption removal of Safranin dye contaminants from water using various types of natural zeolite. Silicon 11:1635–1647. https://doi.org/10.1007/s12633-018-9980-3
13. Laskar N, Kumar U (2018) Adsorption of Safranin (cationic) dye from water by Bambusa tulda: characterization and ANN modeling. Environ Eng Sci 35:1361–1375. https://doi.org/10.1089/ees.2017.0532
14. Azimvand J, Didehban K, Mirshokraie SA (2018) Safranin-O removal from aqueous solutions using lignin nanoparticle-g-polyacrylic acid adsorbent: synthesis, properties, and application. Adsorpt Sci Technol 36:1422–1440. https://doi.org/10.1177/0263617418777836
15. Ivanova N, Gugleva V, Dobreva M, et al (2016) We are IntechOpen , the world ' s leading publisher of Open Access books Built by scientists , for scientists TOP 1 %. Intech i:13
16. Vagropoulou G, Trentsiou M, Georgopoulou A et al (2021) Hybrid chitosan/gelatin/nanohydroxyapatite scaffolds promote odontogenic differentiation of dental pulp stem cells and in vitro biomineralization. Dent Mater 37:e23–e36. https://doi.org/10.1016/j.dental.2020.09.021
17. Kaygili O, Dorozhkin SV, Keser S (2014) Synthesis and characterization of Ce-substituted hydroxyapatite by sol-gel method. Mater Sci Eng C 42:78–82. https://doi.org/10.1016/j.msec.2014.05.024
18. Xue C, Chen Y, Huang Y, Zhu P (2015) Hydrothermal synthesis and biocompatibility study of highly crystalline carbonated hydroxyapatite nanorods. Nanoscale Res Lett 10:1–6. https://doi.org/10.1186/s11671-015-1018-9
19. Gentile P, Wilcock CJ, Miller CA et al (2015) Process optimisation to control the physico-chemical characteristics of biomimetic nanoscale hydroxyapatites prepared using wet chemical precipitation. Materials (Basel) 8:2297–2310. https://doi.org/10.3390/ma8052297
20. Suhas GVK, Carrott PJM et al (2016) Cellulose: a review as natural, modified and activated carbon adsorbent. Bioresour Technol 216:1066–1076. https://doi.org/10.1016/j.biortech.2016.05.106
21. Hassan AF, Hrdina R (2018) Chitosan/nanohydroxyapatite composite based scallop shells as an efficient adsorbent for mercuric ions: static and dynamic adsorption studies. Int J Biol Macromol 109:507–516. https://doi.org/10.1016/j.ijbiomac.2017.12.094
22. Abu-Thabit NY, Judeh AA, Hakeem AS et al (2020) Isolation and characterization of microcrystalline cellulose from date seeds (Phoenix dactylifera L.). Int J Biol Macromol 155:730–739. https://doi.org/10.1016/j.ijbiomac.2020.03.255
23. Wang Y, Lindström ME, Henriksson G (2014) Increased degradability of cellulose by dissolution in cold alkali. BioResources 9:7566–7578. https://doi.org/10.15376/biores.9.4.7566-7578
24. Catori DM, Fragal EH, Messias I et al (2021) Development of composite hydrogel based on hydroxyapatite mineralization over pectin reinforced with cellulose nanocrystal. Int J Biol Macromol 167:726–735. https://doi.org/10.1016/j.ijbiomac.2020.12.012
25. Mok CF, Ching YC, Osman NAA, et al (2020) Adsorbents for removal of cationic dye: nanocellulose reinforced biopolymer composites. J Polym Res 27:372–387. https://doi.org/10.1007/s10965-020-02347-3
26. Inyinbor AA, Adekola FA, Olatunji GA (2016) Kinetics, isotherms and thermodynamic modeling of liquid phase adsorption of rhodamine B dye onto Raphia hookeri fruit epicarp. Water Resour Ind 15:14–27. https://doi.org/10.1016/j.wri.2016.06.001
27. Le VT, Doan VD, Nguyen DD, et al (2018) A novel cross-linked magnetic hydroxyapatite/chitosan composite: preparation, characterization, and application for Ni(II) ion removal from aqueous solution. Water Air Soil Pollut 229:100–114. https://doi.org/10.1007/s11270-018-3762-9
28. Hassan AF, Alafid F, Hrdina R (2020) Preparation of melamine formaldehyde/nanozeolite Y composite based on nanosilica extracted from rice husks by sol–gel method: adsorption of lead (II) ion. J Sol-Gel Sci Technol 95:211–222. https://doi.org/10.1007/s10971-020-05295-y
29. Tan CHC, Sabar S, Hussin MH (2018) Development of immobilized microcrystalline cellulose as an effective adsorbent for methylene blue dye removal. South African J Chem Eng 26:11–24. https://doi.org/10.1016/j.sajce.2018.08.001
30. Hassan AF, Hrdina R (2021) Enhanced removal of arsenic from aqueous medium by modified silica nanospheres: kinetic and thermodynamic studies. Arab J Sci Eng. https://doi.org/10.1007/s13369-021-05357-5
31. Teodoro FS, Elias MMC, Ferreira GMD et al (2018) Synthesis and application of a new carboxylated cellulose derivative. Part III: removal of auramine-O and safranin-T from mono- and bi-component spiked aqueous solutions. J Colloid Interface Sci 512:575–590. https://doi.org/10.1016/j.jcis.2017.10.083
32. Nabili A, Fattoum A, Passas R et al (2014) Extraction and characterization of cellulose from date palm seeds (Phoenix dactylifera L.) Laboratory of Pulp, Paper and Graphic Arts Sciences, UMR CNRS 5518. Cellul Chem Technol 50:9–10
33. Herdocia-Lluberes CS, Laboy-López S, Morales S et al (2015) Evaluation of synthesized nanohydroxyapatite-nanocellulose composites as biocompatible scaffolds for applications in bone tissue engineering. J Nanomater. https://doi.org/10.1155/2015/310935
34. Sarkar C, Chowdhuri AR, Kumar A et al (2018) One pot synthesis of carbon dots decorated carboxymethyl cellulose- hydroxyapatite nanocomposite for drug delivery, tissue engineering and Fe3+ ion sensing. Carbohydr Polym 181:710–718. https://doi.org/10.1016/j.carbpol.2017.11.091
35. Hamad AA, Hassouna MS, Shalaby TI et al (2020) Electrospun cellulose acetate nanofiber incorporated with hydroxyapatite for removal of heavy metals. Int J Biol Macromol 151:1299–1313. https://doi.org/10.1016/j.ijbiomac.2019.10.176
36. Su Y, Wu Y, Liu M et al (2020) Ferric ions modified polyvinyl alcohol for enhanced molecular structure and mechanical performance. Materials (Basel) 13:1–13. https://doi.org/10.3390/ma13061412
37. Skwarek E, Goncharuk O, Sternik D, et al (2017) Synthesis, structural, and adsorption properties and thermal stability of nanohydroxyapatite/polysaccharide composites. Nanoscale Res Lett 12:155–167. https://doi.org/10.1186/s11671-017-1911-5
38. Rajkumar M, Meenakshisundaram N, Rajendran V (2011) Development of nanocomposites based on hydroxyapatite/sodium alginate: synthesis and characterisation. Mater Charact 62:469–479. https://doi.org/10.1016/j.matchar.2011.02.008
39. Zadegan S, Hossainalipour M, Ghassai H et al (2010) Synthesis of cellulose-nanohydroxyapatite composite in 1-n-butyl-3- methylimidazolium chloride. Ceram Int 36:2375–2381. https://doi.org/10.1016/j.ceramint.2010.07.019
40. Pieper CM, da Rosa WLO, Lund RG et al (2020) Biofilms of cellulose and hydroxyapatite composites: alternative synthesis process. J Bioact Compat Polym 35:469–478. https://doi.org/10.1177/0883911520951838
41. Ahangaran F, Hassanzadeh A, Nouri S (2013) Surface modification of Fe3O4@SiO2 microsphere by silane coupling agent. Int Nano Lett 3:3–7. https://doi.org/10.1186/2228-5326-3-23
42. Sahu MK, Patel RK (2015) Removal of safranin-O dye from aqueous solution using modified red mud: kinetics and equilibrium studies. RSC Adv 5:78491–78501. https://doi.org/10.1039/c5ra15780c
43. Bello OS (2013) Adsorptive removal of malachite green with activated carbon prepared from oil palm fruit fibre by KOH activation and CO2 gasification. South African J Chem 66:32–41
44. Laskar N, Kumar U (2017) SEM, FTIR and EDAX Studies for the removal of Safranin dye from water bodies using

modified biomaterial - Bambusa tulda. IOP Conf Ser Mater Sci Eng 225:012105. https://doi.org/10.1088/1757-899x/225/1/012105
45. Tan KB, Abdullah AZ, Horri BA, Salamatinia B (2016) Adsorption mechanism of microcrystalline cellulose as green adsorbent for the removal of cationic methylene blue dye. J Chem Soc Pakistan 38:651–664
46. Başaran Kankılıç G, Metin AÜ (2020) Phragmites australis as a new cellulose source: extraction, characterization and adsorption of methylene blue. J Mol Liq 312:113313–113323. https://doi.org/10.1016/j.molliq.2020.113313
47. Hassan AF (2019) Synthesis of carbon nano-onion embedded metal–organic frameworks as an efficient adsorbent for cadmium ions: kinetic and thermodynamic studies. Environ Sci Pollut Res 26:24099–24111. https://doi.org/10.1007/s11356-019-05581-5
48. Kamal KH, Dacrory S, Ali SSM et al (2019) Adsorption of Fe ions by modified carrageenan beads with tricarboxy cellulose: kinetics study and four isotherm models. Desalin Water Treat 165:281–289. https://doi.org/10.5004/dwt.2019.24560
49. Joudi M, Nasserlah H, Hafdi H et al (2020) Synthesis of an efficient hydroxyapatite–chitosan–montmorillonite thin film for the adsorption of anionic and cationic dyes: adsorption isotherm, kinetic and thermodynamic study. SN Appl Sci 2:1–13. https://doi.org/10.1007/s42452-020-2848-3
50. Acemioğlu B, Bilir MH, Alma MH (2018) Adsorption of safranin-O dye by peanut shell-based polyurethane type foam. Int J Chem Technol 2:95–104. https://doi.org/10.32571/ijct.454516
51. Dakhil Nassir Taha IS (2013) Adsorptive removal of dye from industrial effluents using natural Iraqi palygorskite clay as low-cost adsorbent. J Asian Sci Res 3:945–955
52. Chandane V, Singh VK (2016) Adsorption of safranin dye from aqueous solutions using a low-cost agro-waste material soybean hull. Desalin Water Treat 57:4122–4134. https://doi.org/10.1080/19443994.2014.991758
53. Ajaelu CJ, Nwosu V, Ibironke L, Adeleye A (2018) Adsorptive removal of cationic dye from aqueous solution using chemically modified African border tree (Newbouldia laevis) bark. J Appl Sci Environ Manag 21:1323. https://doi.org/10.4314/jasem.v21i7.18
54. Fayazi M, Afzali D, Taher MA et al (2015) Removal of Safranin dye from aqueous solution using magnetic mesoporous clay : optimization study. J Mol Liq 212:675–685. https://doi.org/10.1016/j.molliq.2015.09.045